Available online at www.sciencedirect.com
ScienceDirect
Trans. Nonferrous Met. Soc. China 35(2025) 2036−2048
Transactions of Nonferrous Metals Society of China
www.tnmsc.cn

Oxidative volatilization mechanism and kinetics of stibnite at low temperature

Jiang LIU[1], Chao-bo TANG[1], Qiang ZHU[1], Jian-guang YANG[1], Tian-xiang NAN[1,2], Xian-pan ZHANG[1]

1. School of Metallurgy and Environment, Central South University, Changsha 410083, China;
2. Department of Chemical and Metallurgical Engineering, School of Chemical Engineering, Aalto University, Vuorimiehentie 2, P.O. Box 16200, FI-00076 Aalto, Finland

Received 6 November 2023; accepted 20 July 2024

Abstract: The substitution of traditional blast furnaces with steel-belt furnaces for antimony smelting was proposed. The influence of various parameters on the oxidative volatilization of stibnite was studied according to the production practice of steel-belt furnaces. Furthermore, the kinetics of oxidative volatilization was elucidated using differential thermal gravimetric analyses and non-isothermal analysis methods. The results indicated that the oxygen concentration and the temperature were pivotal variables in the oxidative volatilization process. Notably, the volatilization efficiency of antimony was 97.25% under optimal conditions. Moreover, the kinetic control stages were divided into chemical reaction control (440−490 °C), internal diffusion control (500−550 °C), and chemical reaction control (560−580 °C). These stages corresponded to activation energies of 16.40−18.79, 120.86−195.96, and 24.00−28.31 kJ/mol, respectively.
Key words: stibnite; oxidative roasting; volatile roasting; kinetics; Coats−Redfern equation

1 Introduction

Antimony is primarily used for the production of alloys, semiconductors, and battery materials [1,2]. Stibnite is the main raw material for antimony smelting. Currently, the dominant method for the extraction of antimony is oxidative volatilization in the blast furnace followed by reductive smelting in the reductive furnace [3].

However, the volatilization smelting of stibnite in a blast furnace necessitates the maintenance of high temperatures (exceeding 1200 °C) to facilitate the rapid volatilization of soot and ensure the unimpeded flow of slag [4]. Concurrently, specific quantities of calcium and iron compounds must be fed into the furnace to reduce the melting point of slag, thereby resulting in the massive production of waste slag [5]. Furthermore, industrial production demonstrates that non-volatile antimony matte and crude antimony tend to be generated in melting, which is the main reason for the low volatility of Sb [6]. Additionally, the energy required for the blast furnace predominantly derives from coke combustion, which liberates considerable volumes of CO_2, thereby exacerbating environmental concerns [7]. In summary, the traditional process poses significant challenges in aligning with stringent global environmental standards, underscoring the imperative need for devising an environmentally benign alternative.

In recent years, steel-belt furnaces have garnered increased interest owing to their simple structure, low energy consumption, and controllable atmosphere [8−10]. The energy for the steel-belt furnaces is electricity, thus the emission of CO_2 can

Corresponding author: Chao-bo TANG, Tel: +86-13875802550, E-mail: 204165@csu.edu.cn
https://doi.org/10.1016/S1003-6326(25)66799-9

be significantly reduced [11]. Notably, unlike in blast furnaces, the vertical flow of the material does not need to be considered for the production process in steel belt furnace since the belt furnace is placed horizontally (see Fig. 1). This means that calcium and iron oxides no longer need to be added to form slag during the production, thereby markedly diminishing the production of hazardous slag. However, documentation on the employment of steel-belt furnaces to treat stibnite is scant. This is because the material must be kept solid to prevent the slag bonding to the steel belt. Nevertheless, as mentioned above, the mainstream volatile roasting processes for stibnite are mostly carried out in the molten state, which is obviously unfeasible for steel-belt furnaces. Hence, how to decrease the volatile roasting temperature of stibnite seems to be a key point.

The potential products during the volatile roasting of stibnite include Sb_2S_3, Sb_2O_3, Sb_2O_4, SbO_2, and Sb, among which Sb_2O_4, SbO_2, and Sb exhibit negligible vaporization at atmospheric pressure below 800 °C [12,13]. ZHOU et al [13] successfully demonstrated the efficient extraction of antimony sulfide from stibnite utilizing vacuum metallurgy techniques, revealing that the saturated vapor pressure of Sb_2O_3 is higher than Sb_2S_3 at the identical temperature. Therefore, promoting the generation of Sb_2O_3 by controlling some conditions in the roasting process is an effective approach for decreasing the temperature of volatile roasting. Moreover, ŽIIVKOVIĆ et al [14] found that the oxidation product of stibnite was easily volatile Sb_2O_3 at oxygen concentrations of 1 vol.% to 5 vol.%. When at oxygen concentrations higher than 5 vol.%, stibnite was oxidized to solid SbO_2 that can decompose to Sb_2O_3 and O_2 over 1150 °C. QIN et al [15] investigated the volatilization mechanism of stibnite in an inert atmosphere. The results showed that stibnite was volatilized as Sb_2S_3 below 900 °C and then decomposed to antimony and sulfur above 900 °C.

For the roasting kinetics of stibnite, PADILLA et al [16] suggested that the roasting product of stibnite was solid Sb_2O_3 in the temperature range of 300−500 °C, the surface reaction is the controlled step, and the temperature and the pressure of oxygen significantly affected the oxidation rate of stibnite. Furthermore, stibnite can be oxidized to Sb, Sb_2O_3, and H_2S by water steam, and the mass transfer step in the gas boundary layer controls the reaction [17]. Regrettably, studies focusing on the volatile roasting kinetics of stibnite remain sparse. Different from other sulfide ores, the roasting product of stibnite in the weak oxygen atmosphere is Sb_2O_3 with significant temperature-dependent volatility, so the kinetic control steps may vary at different temperatures. Consequently, elucidating the kinetic mechanism of oxidative volatilization of stibnite under variable conditions holds substantial scientific value.

In this work, the effects of oxygen concentration, temperature, layer thickness, and ore particle size on the volatilization of stibnite were studied based on the actual production of steel-belt furnaces. Subsequently, the roasting kinetic of stibnite, with variations in particle size and temperature, was studied through thermo-gravimetric in conjunction with Coats−Redfern functions. These findings illuminate the regulatory effect of various parameters on the volatilization rate of Sb and disclose the kinetic mechanism of

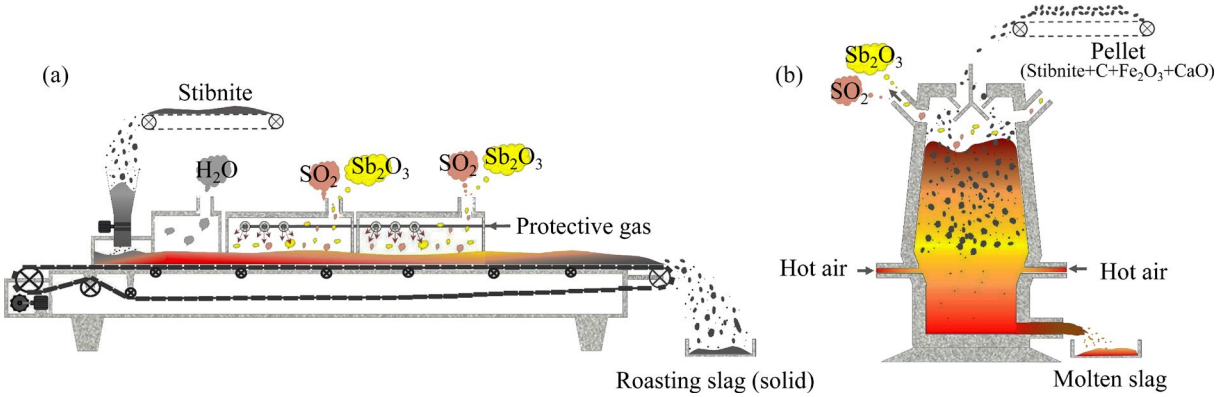

Fig. 1 Schematic diagram for volatile roasting of stibnite in steel-belt furnace (a) and in blast furnace (b)

the oxidative volatilization process. The outcome of this investigation offers invaluable guidance for the environmentally conscientious roasting of stibnite.

2 Experimental

2.1 Materials

The stibnite used in this study was obtained from Hunan Chenzhou Mining Group, China. The chemical and phase composition are shown in Table 1 and Fig. 2, respectively. The results suggest that the main elements in stibnite are Sb (29.2 wt.%), S (28.59 wt.%), As (0.94 wt.%), Fe (10.59 wt.%), and Si (12.99 wt.%). The main phases in stibnite are Sb_2S_3, FeS_2, and SiO_2. In addition, the purity of both nitrogen and oxygen used during the experiment was higher than 99.99 vol.%.

Table 1 Chemical composition of raw materials (wt.%)

Sb	S	As	Fe	Si	O
29.20	28.59	0.94	10.59	12.99	14.68
Al	Zn	Pb	Ca	Others	
1.93	0.49	0.30	0.21	0.08	

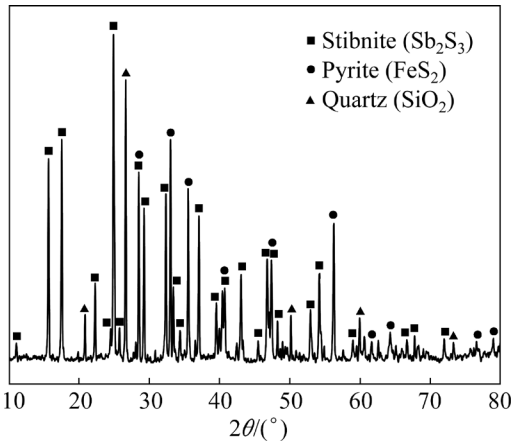

Fig. 2 XRD pattern of stibnite

2.2 Method

2.2.1 Oxidized volatile roasting process

In the roasting experiments, 5 g of stibnite was loaded into an alumina crucible and spread to a given thickness (measured by a steel ruler). Subsequently, the crucible was pushed into the constant temperature zone of the tube furnace (see Fig. 3). After exhausting the air by nitrogen−oxygen gas mixture (1 L/min for 10 min), the heating system was switched on according to a pre-set procedure, and the heating rate was 7 °C/min. The mixture gas of nitrogen and oxygen was continuously fluxed during the reaction. After the required roasting time, the crucible was taken out and quickly quenched in liquid nitrogen and weighed. The volatiles were collected in the glass bottle and the ends of the furnace tube.

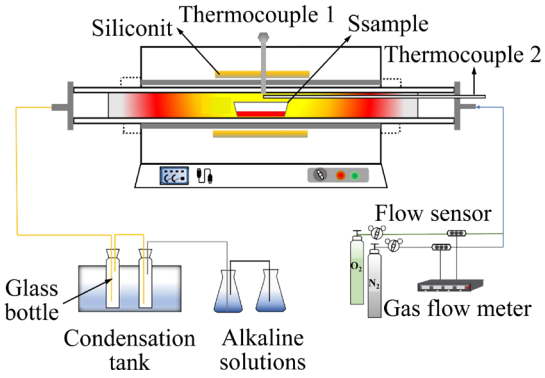

Fig. 3 Schematic diagram of experimental apparatus

X-ray diffractometer (XRD, D/max 2550PC, Rigaku Ltd; Japan) was applied to determining the phase composition in roasting slag and volatiles. The data were collected in the 2θ of 10°−80° with the scan rate of 10 (°)/min. ICP-AES (ICP-AES, Perkin Elmer, Optima 3000; Norwalk, USA) was employed to detect the content of Sb in the roasting slag. The volatilization efficiency of Sb (η) was calculated based on Eq. (1):

$$\eta = \left(1 - \frac{m_1 w'_{Sb}}{m_0 w_{Sb}}\right) \times 100\% \quad (1)$$

where m_0 and m_1 are the mass (g) of the raw ore and roasting slag, respectively, and w_{Sb} and w'_{Sb} are the mass fraction of Sb in the raw ore and roasting slag, respectively.

2.2.2 Kinetics of oxidative volatilization roasting

In kinetic experiments, a small amount of stibnite was analyzed using TG-DSC (Universal V4.0C TA instrument with SDT Q600 V8.0 Build 95) at a heating rate of 7 °C/min and the N_2 and O_2 mixture gas (oxygen concentration 1 vol.%) flow of 100 mL/min from 25 to 900 °C. Afterward, the TG-DSC data were taken into specific equations to obtain kinetic parameters. For verifying the calculated results, X-ray diffractometer (XRD, D/max 2550PC, Rigaku Ltd; Japan) was applied to determining the phase composition of the roasting slag. The data were collected in the 2θ of 10°−80° with the scan rate of 10 (°)/min. The microscopic

features and elemental distribution of the roasting slag were characterized by a scanning electron microscope and energy spectrometer (SEM−EDS, LEO 1450, Carl Zeiss, Germany; EDS, INCA Wave 8570, Oxford Instruments, UK).

In this study, the Coats−Redfern method was adopted to carry out the kinetic analysis, and its function is expressed as [18,19]

$$\ln\frac{F(x)}{T^2}=\ln\left[\frac{AR}{\beta E}\left(1-\frac{2RT}{E}\right)\right]-\frac{E}{RT} \tag{2}$$

where R is the gas molar constant, β is the rate of temperature rise, E is the activation energy, $F(x)$ is the reaction mechanism function, T is the temperature, x is the oxidation ratio at different temperatures, and A is the frequency factor [20].

In most cases, the activation energy (E) is very large, so the variable amount of $\ln\left[\frac{AR}{\beta E}\left(1-\frac{2RT}{E}\right)\right]$ is very small [21]. For a given reaction, the relationship between $\ln[F(x)/T^2]$ and $1/T$ can be obtained by calculation, and the values of E and A can be calculated from the slope and intercept of the fitted line.

As for the reaction mechanism function ($F(x)$), the experimental phenomenon revealed that the slag is solid after roasting, so the unreacted shrink nucleus model of gas−solid reaction can be applied, and the kinetics equations of different control steps are given in Table 2.

Table 2 Kinetics equations of shrinking core model at different control steps [22]

Function	Kinetic equation	Control step
$F_1(x)$	$1-(1-x)^{1/3}=k_1t$	Chemical reaction control
$F_2(x)$	$1-(1-x)^{2/3}=k_2t$	External diffusion control
$F_3(x)$	$1-2x/3-(1-x)^{2/3}=k_3t$	Internal diffusion control

t (min) is the reaction time, and k is the reaction rate constant

3 Results and discussion

3.1 Thermodynamic calculation

The thermodynamic diagram of the Sb−S−O system at different temperatures is shown in Fig. 4. The red lines in Fig. 4 are 101.325 kPa isobar.

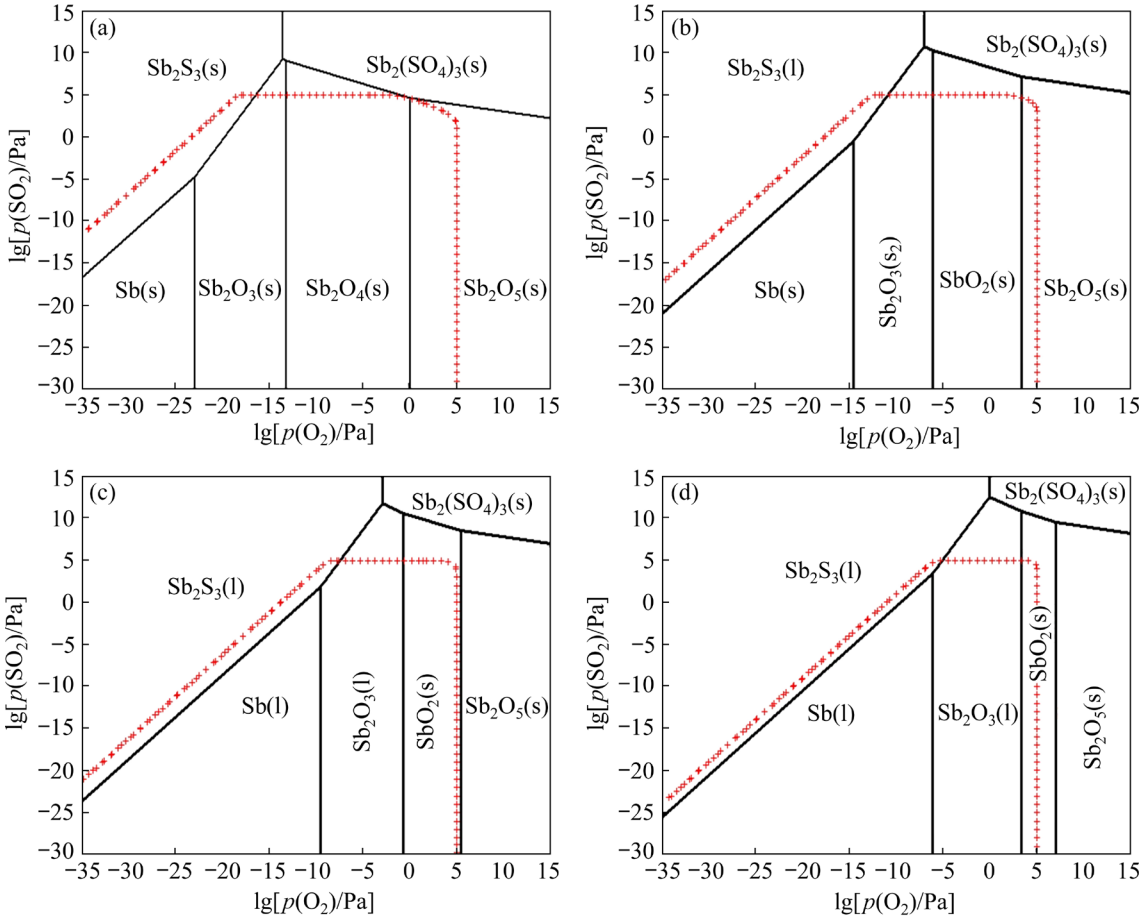

Fig. 4 Thermodynamic diagrams of Sb−S−O system at different temperatures: (a) 400 °C; (b) 600 °C; (c) 800 °C; (d) 1000 °C

The results show that as the oxygen potential increases at 400 °C, the stabilization products are Sb_2S_3(s), Sb_2O_3(s), Sb_2O_4(s), and Sb_2O_5(s) sequentially at 101.325 kPa. When the temperature is increased to 600 °C, Sb_2O_4(s) is converted to SbO_2(s), and the conversion sequence of materials with oxygen concentration at this temperature (101.325 kPa) is similar to that at 400 °C. It is worth noting that Sb_2O_4(s), SbO_2(s), and Sb_2O_5(s) are difficult to volatilize, so a proper oxygen concentration should be controlled to avoid their generation [23,24]. Besides, above 800 °C, Sb_2O_5(s) is difficult to generate at 101.325 kPa, and the phase transformation path with increasing oxygen concentration is (101.325 kPa) Sb_2S_3(s), Sb_2O_3(s), SbO_2(s). Figure 4 also indicates that $Sb_2(SO_4)_3$(s) is not able to be formed in the temperature range of 400−1000 °C at 101.325 kPa.

Furthermore, as shown in Fig. 4, the stability zone of Sb_2O_3 shifts to the right with increasing temperature, which means that raising temperature can increase the oxygen partial pressure for the oxidative volatilization roasting of antimony sulfide, which is beneficial for controlling oxygen concentration in industrial.

3.2 Oxidative volatilization of stibnite

The roasting atmosphere, temperature, layer thickness, roasting time (controlled by the moving rate of the belt), material particle size, and gas flow rate are crucial for steel-belt furnaces [11]. Therefore, the effect of these factors on the oxidative volatilization was investigated.

3.2.1 Effect of oxygen concentration

The effect of oxygen concentration on the volatilization efficiency of Sb was studied at the roasting temperature of 800 °C, the layer thickness of 2 mm, the roasting time of 75 min, the material size of 96−150 μm, and the mixture gas flow rate of 1000 mL/min. The results (Fig. 5(a)) show that the volatilization efficiency of Sb decreased with the increasing oxygen concentration. The volatilization efficiency of Sb was above 95% below 5 vol.%. However, the volatilization efficiency of Sb decreased significantly above 7 vol.% oxygen and dropped to 86.99% at 9 vol.% oxygen.

The XRD patterns of the roasting slag are shown in Fig. 6. The results indicate that the main phases in the roasting slag are SiO_2 and Fe_2O_3 below 5 vol.%. The peaks of Sb_2O_4 and $FeSbO_4$ (tripuhyite) [25] were detected at 7 vol.%. Moreover, as the oxygen concentration rises, the peak intensity of $FeSbO_4$ was significantly enhanced, but the peak intensity of Fe_2O_3 and Sb_2O_4 was reduced. This means that the increase in oxygen concentration promotes the reaction between Sb_2O_4 and Fe_2O_3 to form $FeSbO_4$ (Reaction (3)) [23]. Overall, the oxygen concentration for oxidative volatilization of stibnite

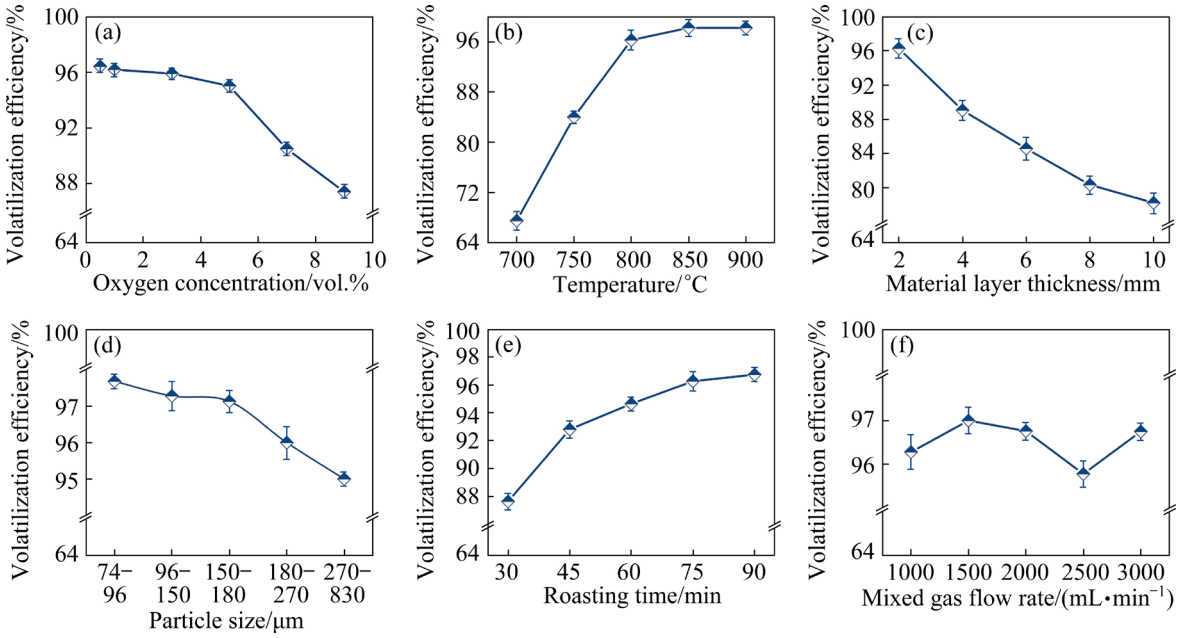

Fig. 5 Effect of different parameters on volatilization efficiency of Sb: (a) Oxygen concentration; (b) Temperature; (c) Material layer thickness; (d) Particle size; (e) Roasting time; (f) Mixed gas flow rate

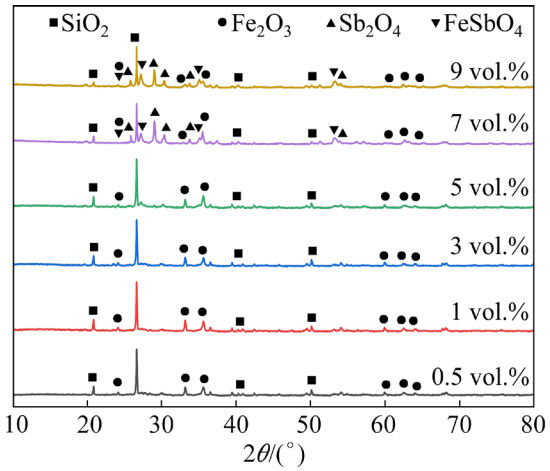

Fig. 6 XRD patterns of roasting slag at different oxygen concentrations

should be below 5 vol.%.

$$2Sb_2O_4+2Fe_2O_3+O_2=4FeSbO_4 \quad (3)$$

3.2.2 Effect of temperature

The relationship between roasting temperature and volatilization efficiency of Sb is shown in Fig. 5(b). Other conditions were the oxygen concentration of 1vol.%, the layer thickness of 2 mm, the material particle size of 96−150 μm, the roasting time of 75 min, and the mixed gas flow rate of 1000 mL/min.

The results indicate that the volatilization efficiency of Sb increases with the rise of roasting temperature. The volatilization efficiency of Sb at 700 and 800 °C were 67.85% and 97.25% respectively. This is because the vapor of the generated Sb_2O_3 is low at 700 °C, which hindered the oxidation of Sb_2S_3 [13]. When the temperature reached 800 °C, the oxidation rate of Sb_2S_3 was accelerated, and the vapor pressure of Sb_2O_3 increased significantly, so the volatilization rate of Sb was increased. Above 800 °C, increasing the temperature results in a slight change in the volatilization efficiency of Sb, but the increased temperature means high energy consumption. Thus, the roasting temperature is determined to be 800 °C.

3.2.3 Effect of material layer thickness

The material layer thickness is an essential factor for steel-belt furnaces, which greatly determines the mass transfer, heat transfer, and production capacity. Thus, the effect of material layer thickness on the roasting process was investigated at 800 °C, and other parameters are the same in previous experiments.

The results (Fig. 5(c)) suggest that the volatilization efficiency of Sb decreased sharply with the increase of the layer thickness. The volatilization efficiency of Sb was 97.23% and 78.66% at 2 and 10 mm, which can be explained in two ways. First, the increase in layer thickness would lead to insufficient contact between the bottom stibnite and the mixed gas, which is unfavorable to the conversion of Sb_2S_3 to Sb_2O_3. Second, the excessive layer thickness hindered the volatilization of Sb_2O_3 produced at the bottom. Thus, the thickness of the layer is found to be 2 mm.

3.2.4 Effect of particle size

Figure 5(d) shows the effect of stibnite particle size on the volatilization efficiency of Sb. Other conditions were the oxygen concentration of 1 vol.%, the roasting temperature of 800 °C, the layer thickness of 2 mm, the roasting time of 75 min, and the mixture gas flow rate of 1000 mL/min.

The results demonstrate that the volatilization efficiency of Sb increased with the reduction of particle size in the range of 150−830 μm. When the material particle size was smaller than 150 μm, the volatilization efficiency of Sb increased little with the decrease in particle size. The finer particle size of Sb_2S_3 corresponds to a lower ignition temperature, so it is conducive to the oxidative volatilization of stibnite [5]. Moreover, the small particle size means large reaction area, which can also promote the oxidative evaporation of stibnite. Besides, the large material size tends to cause the encapsulation of unreacted nuclei by gangue and prevent the oxidative evaporation of stibnite (see Fig. S1 in Supplementary Information (SI)). The volatilization efficiency of Sb was 97.25% at the particle size of 96−150 μm, and the improvement of the volatilization efficiency of Sb was no longer obvious when the particle size was smaller than 96 μm. Hence, considering the cost of grinding, the optimal range of particle sizes is 96−150 μm.

3.2.5 Effect of roasting time

The control of holding time in the steel-belt furnaces can be performed by adjusting the moving rate of the steel-belt. Roasting time is a critical factor for the yield of steel-belt furnaces.

The effect of roasting time on the volatilization efficiency of Sb was investigated at the oxygen

concentration of 1 vol.%, the roasting temperature of 800 °C, the material layer thickness of 2 mm, the material size of 96 to150 μm, and the mixture gas flow rate of 1000 mL/min, and the results are presented in Fig. 5(e).

Figure 5(e) indicates that prolonging the roasting time is beneficial to the oxidative volatilization of stibnite. The volatilization efficiency of Sb increased from 87.66% to 97.24% when the roasting time was extended from 30 to 90 min. However, the improvement in the volatilization efficiency of Sb by extending the holding time was no longer significant beyond 75 min. This may result from the little generation of antimonate and metallic antimony [26]. Considering the production efficiency and energy consumption, the optimal holding time is 75 min.

3.2.6 Effect of mixed gas flow rate

The effect of mixed gas flow rate on the volatilization efficiency of Sb was investigated based on other optimized parameters, as shown in Fig. 5(f).

The results suggest that the effect of mixed gas flow rate on the volatilization efficiency of Sb is insignificant. The volatilization efficiency of Sb was above 96% in the range of 1000−3500 mL/min and fluctuated with the variations of gas flow rate. Considering the gas mixture consumption and the heat loss in the roasting process, the gas flow rate was selected to be 1000 mL/min.

The optimized parameters for volatilization roasting of stibnite are shown in Table 3. The volatilization efficiency of Sb at the optimized process conditions was 97.25%. Compared to the volatile roasting in the blast furnace, the temperature of this novel process is lowered by about 400 °C [4]. And this novel process does not need auxiliary materials such as coke, iron oxide, and calcium oxide, so the mass of the roasting slag can be drastically reduced. Moreover, the roasting process can take full advantage of the combustion characteristics of the sulfide ore due to the selected thin material layer (2 mm), which will significantly reduce the energy consumption of the roasting process [27]. Furthermore, clean electricity can be used as an energy supplement for the roasting process to reduce CO_2 emissions significantly.

3.3 Characterization of roasting products

Table 4 shows that the elements in the roasting slag are Si (28.74 wt.%), Fe (19.20 wt.%), Al (3.94 wt.%), and Sb (1.87 wt.%). The XRD patterns of the products under the optimized conditions are shown in Fig. 7. The result reveals that the main phases in the roasting slag are SiO_2 and Fe_2O_3. The antimony compounds were not detected in the slag, indicating that the volatilization of Sb was complete at optimal conditions. At the same time, the phases in the volatiles were identified as Sb_2O_3 and $AsSbO_3$. Moreover, as shown in Fig. 7, the roasting slag remained loose and solid after roasting, which satisfied the production requirements of the steel-belt furnace.

3.4 Kinetics of oxidative volatilization

3.4.1 Analysis of TG-DSC curve

The thermogravimetric behavior of stibnite with different grain sizes was studied at the oxygen concentration of 1 vol.%, as shown in Fig. 8.

In Fig. 8, three exothermic peaks were detected in the temperature ranges of 490−530 °C, 530−540 °C, and 560−580 °C. The roasting slag of stibnite (75−96 μm) was analyzed by XRD from 440 to 580 °C to clarify the chemical reactions for each peak, and the results are shown in Fig. 9. The diffraction peaks of Sb_2S_3 and FeS_2 were clearly present at 440 °C, which indicates that the stibnite is almost unreacted at 440 °C. Then, the peak of Sb_2O_3 was detected at 480 °C and further enhanced at 520 °C. At the same time, the peak intensity of Sb_2S_3 was reduced. Furthermore, the peak intensity of FeS_2 is constant from 440 to 520 °C. Based on the above analysis, an obvious conclusion is that the main reaction between 440 and 520 °C is the oxidation of Sb_2S_3, which corresponds to the first exothermic peak on the DSC curve. Then, the diffraction peak of FeS_2 vanished, and the peak of Fe_2O_3 was detected at 560 °C, which indicated that FeS_2 was oxidized to Fe_2O_3 from 520 to 560 °C. This corresponds to the second exothermic peak on

Table 3 Optimal parameters of roasting process

Oxygen concentration/vol.%	Temperature/°C	Layer thickness/mm	Time/min	Particle size/μm	Flow rate/ ($mL \cdot min^{-1}$)
≤5	800	2	75	≤96	1000

Table 4 Chemical composition of roasting slag (wt.%)

Si	Fe	Al	Sb	As	O
28.74	19.20	3.94	1.87	0.036	45.56

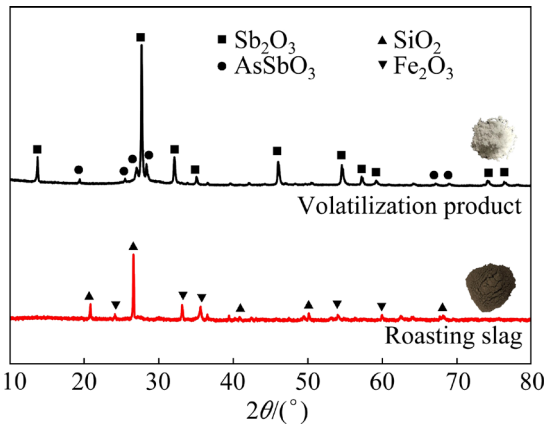

Fig. 7 XRD patterns of roasting slag and volatilization products under optimized conditions

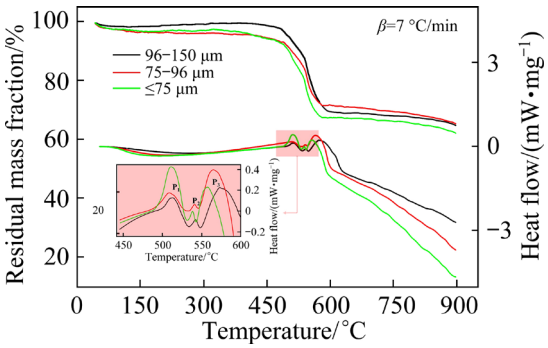

Fig. 8 TG-DSC curves of stibnite with different particle sizes

the DSC curve. Figure 9 also demonstrates that part of Sb_2S_3 is still present at 560 °C, and it would be oxidized at a higher temperature, corresponding to the third exothermic peak of the DSC curve. Besides, Fig. 8 also shows that the slopes of the TG and DSC curves at 900 °C are still negative, which indicates that there is a slow mass loss process that is heat-absorbing in the system. This corresponds to the volatilization of residual Sb_2O_3.

Similarly, three mass loss was observed on TG curves in the temperature ranges of 80−490 °C, 490−580 °C, and 580−900 °C. The mass loss occurred mainly at 490−580 °C, accounting for more than 80% of the total mass loss. Considering the DSC results, it can be inferred that the three mass loss processes corresponded to the evaporation of water in the raw material, the oxidation reaction of Sb_2S_3 and FeS_2, and the volatilization of Sb_2O_3, respectively.

The reaction ratio and reaction rate versus temperature can be calculated [22], and the results are shown in Fig. 10.

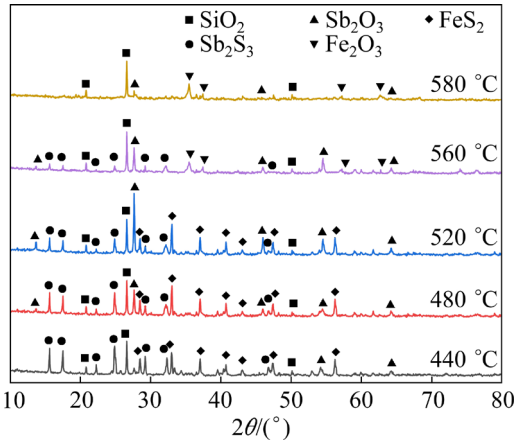

Fig. 9 XRD patterns of roasting slag at different roasting temperatures

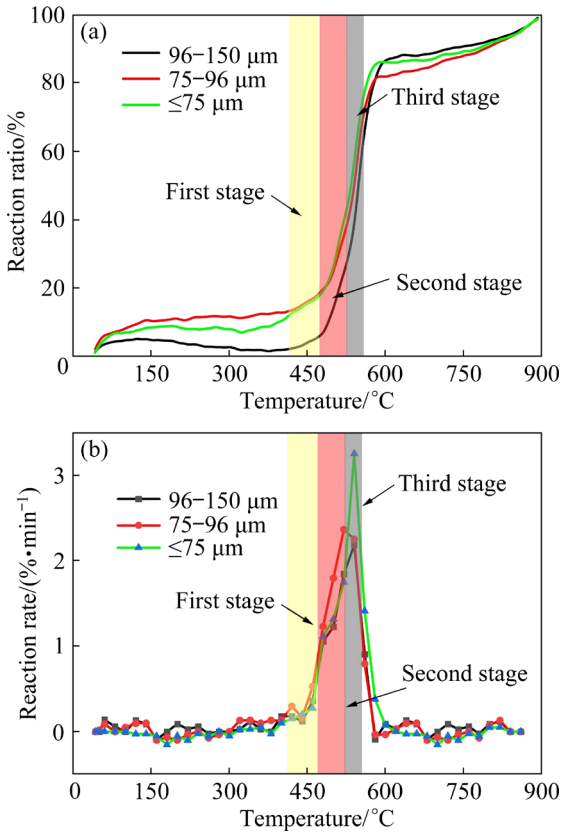

Fig. 10 Reaction ratio (a) and reaction rate (b) at different temperatures

As shown in Fig. 10(a), the oxidation of stibnite started at 400 °C and mainly occurred at 440−580 °C. Figure 10(b) also indicates that the oxidation reaction mainly occurred at 440−580 °C. With the ascent of temperature, the reaction rate

exhibited a progressive acceleration followed by a subsequent deceleration. The oxidization rate of minute stibnite significantly surpassed that of its larger counterpart at a specific temperature. Significantly, the curve of reaction rate vs temperature shows a clear inflection point around 540 °C, which implies that the kinetic step may be transformed at 540 °C [28]. Based on the above analysis, 440−580 °C was adopted as the temperature interval for the kinetic study.

3.4.2 Division of reaction stages

$F(x)$ for different control steps was obtained based on the reaction ratio. Then, $F(x)$ was taken into the Coats−Redfern model to get a curve of $\ln[F(x)/T^2]$ versus $1/T$. Finally, the linear fitting of $\ln[F(x)/T^2]$ to $1/T$ was performed, and the fitting results with different particle sizes are plotted in Fig. 11.

In Fig. 11, two distinct inflection points were observed at about $1/T=12\times10^{-4}$ and 13×10^{-4} K^{-1}. Next, the temperatures corresponding to these two inflection points were calculated as 490 and 550 °C based on the raw data. This implies that the kinetic control steps may vary across different temperature ranges. Therefore, the reaction process can be divided into three stages based on two inflection points. In addition, in order to eliminate the impact of the transition of the kinetic control step on the experimental results, the reaction was divided into three stages: the first stage (440−490 °C), the second stage (500−550 °C), and the third stage (560−580 °C).

The fitting results of $\ln[F(x)/T^2]$ and $1/T$ for the three stages are listed in Table 5. where E_a is the activation energy of the reaction, A is the preexponential factor, and R^2 is the linear correlation coefficient. It is found that the correlation is great after linear treatment, which further proves the rationalization of the reaction division.

SEM−EDS analyses of the roasting slag (Obtained from the roasting process in a tube furnace) at 470, 530, and 570 °C were performed to visualize the kinetic transition process, and the results are shown in Fig. 12. The results reveal that the roasting products can be divided into two types, corresponding to the bright white and the gray areas in Fig. 12. Based on the EDS surface scanning results, the phases in the bright white and the gray areas were identified as antimony sulfide and antimony oxide, respectively.

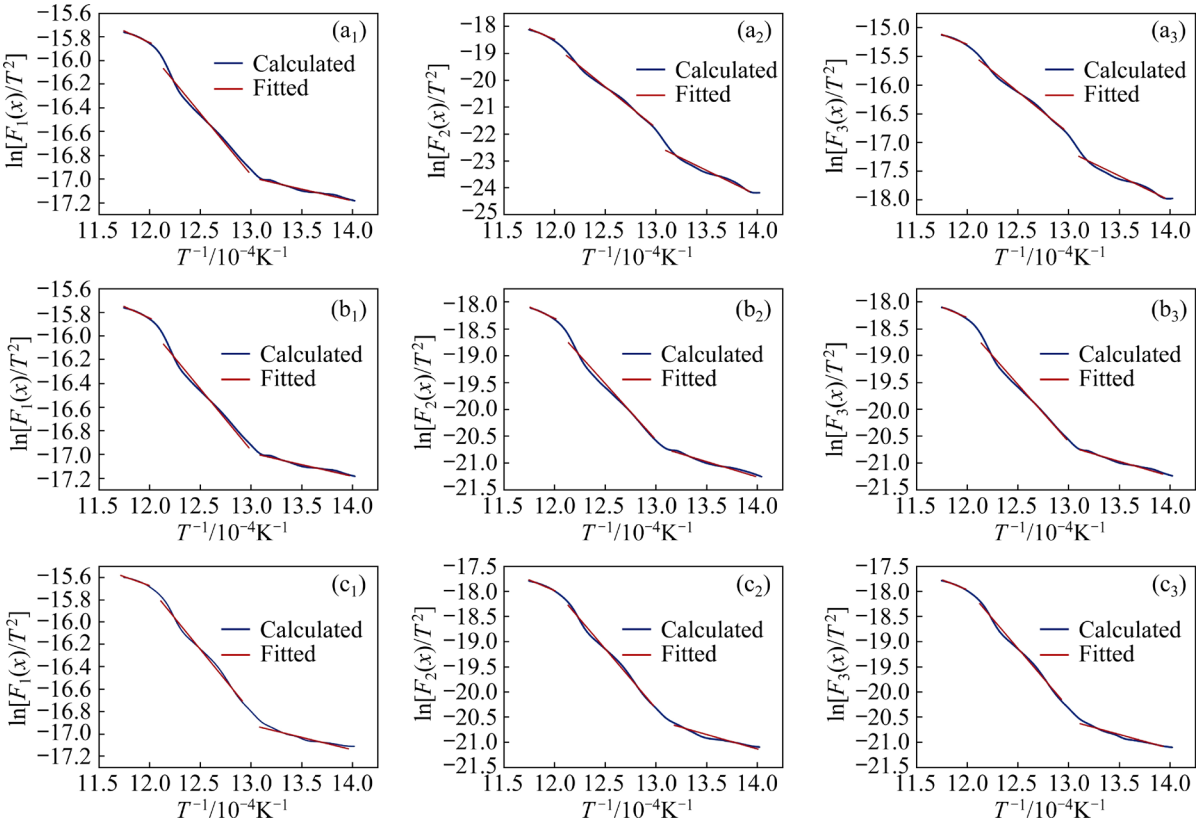

Fig. 11 Linear fitting results of $\ln[F(x)/T^2]$ vs $1/T$ at different control steps with different particle sizes: (a_1−a_3) 96−150 μm; (b_1−b_3) 75−96 μm; (c_1−c_3) ≤75 μm

Table 5 Kinetic parameters of oxidation process of stibnite

Particle size/μm	Kinetic function	The first stage			The second stage			The third stage		
		E_a/(kJ·mol^{-1})	A	σ^2	E_a/(kJ·mol^{-1})	A	σ^2	E_a/(kJ·mol^{-1})	A	σ^2
96−150	$F_1(x)$	16.46	0.000523	0.933	86.51	46.38	0.976	28.31	0.00621	0.968
	$F_2(x)$	152.75	9781.46	0.978	256.63	3551700.89	0.989	126.3	1564.2	0.973
	$F_3(x)$	70.15	2.4	0.974	120.86	14914.6	0.988	54.99	0.67	0.967
75−96	$F_1(x)$	16.48	0.000523	0.932	86.51	46.38	0.976	28.31	0.00621	0.97
	$F_2(x)$	45.11	0.00104	0.965	180.92	5808945.18	0.982	71.26	0.411	0.985
	$F_3(x)$	44.82	0.000995	0.963	182.93	7949929.41	0.98	67.69	0.237	0.981
≤75	$F_1(x)$	18.79	0.000663	0.872	93.538	174.32	0.989	24	0.0041	0.964
	$F_2(x)$	47.31	0.000412	0.912	235.14	25662566.2	0.962	88.43	0.0833	0.963
	$F_3(x)$	49.39	0.00246	0.924	195.96	89639094.2	0.99	58.84	0.0841	0.978

σ^2 is the variance

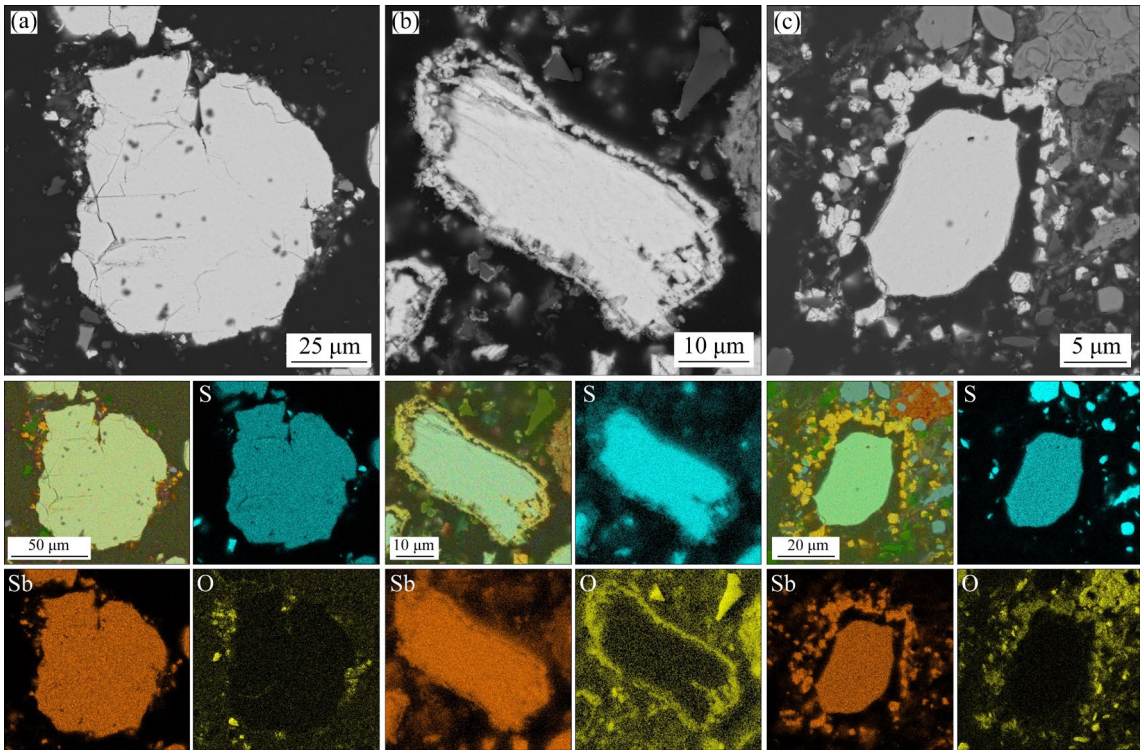

Fig. 12 SEM-EDS results of roasting slag of stibnite (75−96 μm) at different roasting temperatures: (a) 470 °C; (b) 520 °C; (c) 570 °C

The gas flow rate during the thermo-gravimetric experimental test was substantial, thereby negating external diffusion as the controlling step for the reaction. Figure 12(a) indicates that the main composition of the roasting slag was unreacted stibnite at 470 °C, and only a thin layer of antimony oxide was generated on the surface of stibnite. Therefore, at this temperature, O_2 and SO_2 could easily pass through the product layer. Furthermore, Fig. 10(b) suggests that the oxidation rate of stibnite was slow at 440−490 °C, and there is no obvious exothermic peak in the DSC curve. Thus, the roasting process was controlled by the chemical reaction at this stage.

When the temperature increased to 500−550 °C, an obvious mass loss and an exothermic peak were observed on the TG-DSC curve (Fig. 8). At the same time, the reaction rate (Fig. 10(b)) rose significantly in the temperature range of 500−550 °C, which resulted in the massive

generation of Sb_2O_3. However, the volatility of Sb_2O_3 was poor in this temperature range, so the unreacted stibnite was encapsulated by the product (see Fig. 12(b)), which retarded the mass transfer of O_2 and SO_2, so the control step of the reaction was converted from chemical reaction control to internal diffusion control.

Within the temperature range from 560 to 580 °C, an obvious exothermic peak appeared on the DSC curve. Meanwhile, Fig. 12(c) shows that the particle size of stibnite decreased obviously, and the oxide layer on the surface of stibnite became loose and crushed. This is due to the gradual volatilization of the roasting products with increasing temperature and time. Furthermore, the increased temperature promoted the combustion of antimony sulfide, which led to a sharp rise in temperature at the reaction interface. Thus, the volatilization rate of the oxidation products on the surface of stibnite was dramatically accelerated. As the evaporation of the oxidation product, the wrap of the reaction product to unreacted nuclei was unpacked over 560 °C, which converted the reaction control step from internal diffusion control to chemical reaction control. By means of the above studies, the kinetic parameters at different stages can be further extracted from Table 5, and the results are shown in Table 6.

In order to further substantiate the reliability of the aforementioned conjecture, the conventional shrinkage-core model has undergone optimization (see Eqs. (S5) and (S9) in SI). Subsequently, the conclusions of the kinetic study were further verified by substituting the data in Table 6 into the optimized equation (see Fig. S2 and Table S1 in SI). Finally, based on the refined equation, the kinetic equations for antimony ore with varying particle sizes were derived as a function of temperature, as depicted in Table 7.

4 Conclusions

(1) At the oxygen concentration below 5 vol.%, temperature of 800 °C, holding time of 75 min, material layer thickness of 2 mm, the mixed gas flow rate of 1000 mL/min, and material particle size of 96−150 μm, the volatilization efficiency of Sb was 97.25%. Oxygen concentration and temperature exert a crucial effect on the volatilization efficiency of Sb. Excessive oxygen concentration (above 5 vol.%) would lead to the generation of Sb_2O_4 and $FeSbO_4$.

(2) The oxidation of stibnite mainly occurs at 440−580 °C. The kinetic control steps of the volatile roasting process can be divided into chemical reaction control stage (440−490 °C), internal diffusion control stage (500−550 °C), and chemical reaction control stage (560−580 °C). The activation energies of these stages are 16.40−18.79, 120.86−195.96, and 24.00−28.31 kJ/mol, respectively.

Table 6 Activation energy and frequency factors at different stages

Particle size/ μm	The first stage		The second stage		The third stage	
	E_{a1}/(kJ·mol^{-1})	A	E_{a2}/(kJ·mol^{-1})	A	E_{a3}/(kJ·mol^{-1})	A
96−150	16.46	0.000523	120.86	14914.60	28.31	0.00621
75−96	16.48	0.000523	182.93	7949929.41	28.31	0.00621
≤75	18.79	0.000663	195.96	89639094.20	24.00	0.00410

Table 7 Summary of kinetic equations under optimization functions

Particle size/ μm	Chemical reaction control (440−490 °C)	Internal diffusion control (500−550 °C)	Chemical reaction control (560−580 °C)
96−150	$1-(1-x)^{1/3}=0.038\exp\{-E_{a1}/[R(T_0+\beta t)]\}\cdot t$	$1-2/3x-(1-x)^{2/3}=0.057\exp\{-E_{a2}/[R(T_0+\beta t)]\}\cdot t$	$1-(1-x)^{1/3}=1.17\exp\{-E_{a3}/[R(T_0+\beta t)]\}\cdot t$
75−96	$1-(1-x)^{1/3}=0.043\exp\{-E_{a1}/[R(T_0+\beta t)]\}\cdot t$	$1-2/3x-(1-x)^{2/3}=0.084\exp\{-E_{a2}/[R(T_0+\beta t)]\}\cdot t$	$1-(1-x)^{1/3}=0.755\exp\{-E_{a3}/[R(T_0+\beta t)]\}\cdot t$
≤75	$1-(1-x)^{1/3}=0.053\exp\{-E_{a1}/[R(T_0+\beta t)]\}\cdot t$	$1-2/3x-(1-x)^{2/3}=0.146\exp\{-E_{a2}/[R(T_0+\beta t)]\}\cdot t$	$1-(1-x)^{1/3}=1.19\exp\{-E_{a3}/[R(T_0+\beta t)]\}\cdot t$

CRediT authorship contribution statement

Jiang LIU: Formal analysis, Methodology, Data curation, Writing – Original draft, Writing – Review & editing; **Chao-bo TANG:** Supervision, Project administration, Funding acquisition, Writing – Review & editing; **Qiang ZHU:** Resources, Investigation, Formal analysis; **Jian-guang YANG:** Supervision, Writing – Review & editing; **Tian-xiang NAN:** Data curation Software, Validation; **Xian-pan ZHANG:** Validation, Conceptualization.

Declaration of competing interest

The authors declare that they have no known competing financial interests or personal relationships that could have appeared to influence the work reported in this paper.

Acknowledgments

This work was supported financially by the National Natural Science Foundation of China (No. 52074362).

Supplementary Information

Supplementary information in this paper can be found at: http://tnmsc.csu.edu.cn/download/21-p2036-2023-1264-Supplementary_Information.pdf.

References

[1] LIU Zhi-ming, SONG T, PAIK U. Sb-based electrode materials for rechargeable batteries [J]. Journal of Materials Chemistry A, 2018, 6(18): 8159−8193.

[2] WANG Zhi-wei, RU Juan-jian, BU Jiao-jiao, HUA Yi-xin, ZHANG Yuan, XU Cun-ying. Direct electrochemical desulfurization of solid Sb_2S_3 to antimony powders in deep eutectic solvent [J]. Journal of the Electrochemical Society, 2019, 166(14): D747−D754.

[3] ANDERSON C G. The metallurgy of antimony [J]. Geochemistry, 2012, 72: 3−8.

[4] YE Long-gang, TANG Chao-bo, CHEN Yong-min, YANG Sheng-hai, YANG Jian-guang, ZHANG Wen-hai. One-step extraction of antimony from low-grade stibnite in sodium carbonate–sodium chloride binary molten salt [J]. Journal of Cleaner Production, 2015, 93: 134−139.

[5] ZHAO Rui-rong, SHI Xi-chang. Physical chemistry of antimony metallurgy [M]. Changsha: Central South University Press, 2003. (in Chinese)

[6] WANG Ke, WANG Qin-meng, CHEN Yuan-lin, LI Zhong-chen, GUO Xue-yi. Antimony and arsenic substance flow analysis in antimony pyrometallurgical process [J]. Transactions of Nonferrous Metals Society of China, 2023, 33(7): 2216−2230.

[7] ZHU Qiang, YANG Jian-guang, TANG Chao-bo, DING Rui-ze, NAN Tian-xiang, HU Qing-chen. One-step electrolytic reduction desulfurization of Sb_2S_3 in different molten salts [J]. Transactions of Nonferrous Metals Society of China, 2023, 33(7): 2206−2215.

[8] WU Gai-hui, LV Han, LONG Miao-gang, HOU Ying-li. Design and application of power battery material steel-belt sinter furnace [J]. Industrial Furnace, 2013, 35(1): 35−38. (in Chinese)

[9] YUAN Feng-yan. The steel-belt type reducing furnace applied in nickel hydroxide reduced by hydrogen [J]. Chemical Engineering Design Communications, 2013, 39(6): 73−74. (in Chinese)

[10] QUADBECK P, STRAUß A, MÜLLER S, KIEBACK B. Atmosphere monitoring in a continuous sintering belt furnace [J]. Journal of Materials Processing Technology, 2016, 231: 406−411.

[11] YU Yang, LI Bao-kuan, WANG Chang-jun, FANG Zheng-zhe, YANG Xiao, TSUKIHASHI F. Evaluation and synergy of material and energy in the smelting process of ferrochrome pellets in steel-belt sintering-submerged arc furnace [J]. Energy, 2019, 179: 792−804.

[12] PADILLA R, RAMÍREZ G, RUIZ M C. High-temperature volatilization mechanism of stibnite in nitrogen-oxygen atmospheres [J]. Metallurgical and Materials Transactions B, 2010, 41(6): 1284−1292.

[13] ZHOU Zhen-gen, LIU Da-chun, XIONG Heng, ZHANG Bo, YANG Bin, DENG Yong, ZHAO Jing-yang. Separation and purification Sb_2S_3 from stibnite by vacuum distillation [J]. Vacuum, 2018, 157: 487−491.

[14] ŽIVKOVIĆ Ž, ŠTRBAC N, ŽIVKOVIĆ D, GRUJIČIĆ D, BOYANOV B. Kinetics and mechanism of Sb_2S_3 oxidation process [J]. Thermochimica Acta, 2002, 383: 137−143.

[15] QIN Wen-qing, LUO Hong-lin, LIU Wei, ZHENG Yong-xing, YANG Kang, HAN Jun-wei. Mechanism of stibnite volatilization at high temperature [J]. Journal of Central South University, 2015, 22(3): 868−873.

[16] PADILLA R, ARACENA A, RUIZ M C. Kinetics of stibnite (Sb_2S_3) oxidation at roasting temperatures [J]. Journal of Mining and Metallurgy, Section B: Metallurgy, 2014, 50(2): 127−132.

[17] HUA Yi-xin, YANG Yong, ZHU Fu-liang. Volatilization kinetics of Sb_2S_3 in steam atmosphere [J]. Journal of Materials Processing Technology, 2003, 19(6): 619−622.

[18] RAZA M, ABU-JDAYIL B, INAYAT A. Pyrolytic kinetics and thermodynamic analyses of date seeds at different heating rates using the Coats−Redfern method [J]. Fuel, 2023, 342: 127799.

[19] ELMAY Y, JEGUIRIM M, TROUVÉ G, SAID R. Kinetic analysis of thermal decomposition of date palm residues using Coats-Redfern method [J]. Energy Sources, Part A: Recovery, Utilization, and Environmental Effects, 2016, 38(8): 1117−1124.

[20] NAQVI S R, UEMURA Y, OSMAN N, YUSUP S. Kinetic study of the catalytic pyrolysis of paddy husk by use of thermogravimetric data and the Coats−Redfern model [J]. Research on Chemical Intermediates, 2015, 41(12): 9743−9755.

[21] SONG Fan-hao, WANG Xiao-jie, LI Ting-ting, ZHANG Jin, BAI Ying-chen, XING Bao-shan, GIESY P J, WU Feng-chang. Spectroscopic analyses combined with Gaussian and Coats−Redfern models to investigate the characteristics and

pyrolysis kinetics of sugarcane residue-derived biochars [J]. Journal of Cleaner Production, 2019, 237: 117855.

[22] TAKASU H, FUNAYAMA S, UCHIYAMA N, HOSHINO H, TAMURA Y, KATO Y. Kinetic analysis of the carbonation of lithium orthosilicate using the shrinking core model [J]. Ceramics International, 2018, 44(10): 11835−11839.

[23] ZHAO Peng-fei, LIU Chen-hui, SRINIVASAKANNAN C, ZHANG Li-bo, WANG Fang, GAO Ji-yun. Basic research on the microwave absorbing properties and microwave roasting mechanism of stibnite concentrate [J]. Powder Technology, 2021, 379: 630−640.

[24] BALAMURUGAN S, ASHIKA S A, SANA FATHIMA T K. Impact of conventional heat treatment on the as-prepared Sb_2O_3 phase materials—Formation of an orthorhombic SbO_2 phase and its characterization studies [J]. Emergent Materials, 2023, 6(4): 1159−1166.

[25] MA Xin-yue, LI Qiao, LI Rui, ZHANG Wei, SUN Xin-yun, LI Jian-sheng, SHEN Jin-you, HANG Wei-qing. Efficient removal of Sb(V) from water using sulphidated ferrihydrite via tripuhyite ($FeSbO_4$) precipitation and complexation [J]. Journal of Environmental Management, 2022, 309: 114675.

[26] ZHU Qiang, YANG Jian-guang, TANG Chao-bo, NAN Tian-xiang, DING Rui-ze, LIU Jiang. Electroreduction of antimony sulfide enhanced by nitrogen bottom blowing in molten NaCl−KCl−Na_2S [J]. JOM, 2022, 74(5): 1889−1899.

[27] WANG Hong-jiang, XU Chao-shui, WU Ai-xiang, AI Chui-ming, LI Xi-wen, Miao Xiu-xiu. Inhibition of spontaneous combustion of sulfide ores by thermopile sulfide oxidation [J]. Minerals Engineering, 2013, 49: 61−67.

[28] LI Xiao-bin, WU Tao, ZHOU Qiu-sheng, QI Tian-gui, PENG Zhi-hong, LIU Gui-hua. Kinetics of oxidation roasting of molybdenite with different particle sizes [J]. Transactions of Nonferrous Metals Society of China, 2021, 31(3): 842−852.

辉锑矿低温氧化挥发机理及动力学研究

刘 将[1]，唐朝波[1]，朱 强[1]，杨建广[1]，南天翔[1,2]，张先盼[1]

1. 中南大学 冶金与环境学院，长沙 410083；

2. Department of Chemical and Metallurgical Engineering, School of Chemical Engineering, Aalto University, Vuorimiehentie 2, P.O. Box 16200, FI-00076 Aalto, Finland

摘 要：采用钢带炉取代传统锑冶炼鼓风炉。根据钢带焙烧炉实际工况研究不同因素对辉锑矿氧化挥发焙烧的影响。此外，通过差热−热重实验和非等温分析法研究氧化挥发动力学。结果表明，氧气浓度和温度是氧化挥发的关键参数。在优化条件下锑的挥发率为 97.25%。动力学控制步骤可分为三个阶段：化学反应控制(440~490 ℃)、内扩散控制(500~550 ℃)和化学反应控制(560~580 ℃)，对应的活化能分别为 16.40~18.79 kJ/mol、120.86~195.96 kJ/mol 和 24.00~28.31 kJ/mol。

关键词：辉锑矿；氧化焙烧；挥发焙烧；动力学；Coats−Redfern 方程

(Edited by Xiang-qun LI)